Mechano-electrochemical modeling of lithium dendrite penetration in a solid-state electrolyte: mechanism and suppression

Chen Lin[a, *], Ling Xiong[a], Haihui Ruan[b, *]

a. Sino-French Institute of Nuclear Engineering and Technology, Sun Yat-Sen University, Zhuhai, China

b. Department of Mechanical Engineering, The Hong Kong Polytechnic University, Hong Kong, China

Abstract

Mechanism of lithium dendrite penetration in solid-state electrolyte (SE) and its suppression strategies are studied based on a new phase field (PF) model involving fracture mechanics, electrodeposition processes, and mechano-electrochemical coupling (MEC) effects. Numerical results reveal high stress-intensity factor is caused by high hydrostatic pressure in lithium and high stiffness of SE does not inhibit dendrite penetration, because the increase in Young's module of SE, E_{SE}, makes stress-intensity factor even more significant. That is the reason why a stiff SE is "pierced" by the much softer lithium dendrites. Considering MEC, the increase in E_{SE} has a competing effect on dendrite penetration causing a nonmonotonic change in dendrite length, which provides a window to mitigate dendrite penetration. Dendrite

* Corresponding author Tel.: + 86 15319738241, E-mail address: linch67@mail.sysu.edu.cn

* Corresponding author Tel.: + 852 2766 6648, Fax: +852 2365 4703, E-mail address: haihui.ruan@polyu.edu.hk

suppression by toughening SE is quantitatively evaluated. A critical fracture surface energy density of SE (γ = 3.5 J m^{-2}) is determined. When γ > 3.5 J m^{-2}, facture toughness becomes larger than stress-intensity factor and dendrite penetration is suppressed with E_{SE}. However, toughening is difficult. Engineering compressive traction, F_a, in SE surfaces is a more realistic strategy, that cause a significantly inhibition in dendrite penetration with F_a from 0 to 100 MPa.

Keyword: Mechano-electrochemical modeling; Lithium dendrite penetration; Solid-state electrolyte

1 **Nomenclature**

ϕ	Order parameter, ϕ = 1 represent the cracks filled with lithium, ϕ = 0 the defect-free SE
g(ϕ)	Double-well function to ensure that both defect and defect-free regions are stable
$h(\phi)$	Interpolation function that varies from one to zero across the interface
θ	Angle between normal direction of interface and the nominal axis of system
ψ^{mech}	Elastic energy density
$a_{\mathrm{R\ (or\ P)}}$	Activity of reactants (or products)
$\mu^{\mathrm{ex}}_{\mathrm{R\ (or\ P)}}$	Excess chemical potential of reactants (or products)
$\varphi_{\mathrm{SE\ (or\ S)}}$	Electrostatic potential in SE (or deposit)
$\boldsymbol{\sigma}$	Stress tensor
μ_{Li}	Chemical potential of lithium
K_{I}	Stress intensity factor for type I cracking
∇	Gradient operator
∂	Partial differential symbol

2

1. Introduction

Solving energy crisis and improving the range and endurance of energy sources require the development of battery technologies. Nowadays, lithium metal batteries (LMBs) are still the leading energy storage solution, because the lithium metal has a high theoretical capacity (3860 mAh g^{-1}) and a low electrode potential (−3.040 V versus standard hydrogen electrode) [1]. For example, at the end of 2018, the United States had 862 MW/1236 MWh of grid-scale battery storage with LMBs dominating over 90% of operating capacity [2].

However, the wide-spread usage of LMBs incurs many safety concerns such as short-circuit and firing, both associated with the use of liquid electrolytes. Short-circuit is induced by lithium dendrites nucleate on the surface of an anode and pierce the separator to cause internal short circuit [3, 4]. They may also penetrate a battery pack to induce toxic leakage. In addition, the low ignition and low boiling points of liquid electrolyte induces the threat of thermal runaway when the battery is overcharged and discharged [5 – 7]. Narrow working temperature, decomposition under high voltage (above 4.5 V), and the inability to suppress heterogeneous lithium deposition make the liquid electrolytes no longer competent for future batteries requiring ultrahigh energy density and charging rate [8]. These problems are reasons for the development of all-solid-state batteries (ASSBs) based on a non-flammable solid-state electrolyte (SE) possessing an ionic conductivity (e.g., over 10^{-4} S cm^{-1}) comparable to that of liquid electrolytes. SE are chemically more stable than liquid electrolytes and has the mechanical resistance towards suppressing non-uniform lithium growth [9 – 11]. In addition,

the use of ASSB eliminates the presence of liquid substances, porous separators, and cooling systems, reduces the number of current collectors, and makes a battery pack assembly simpler and cheaper.

Most SE have a shear modulus of the order of 10 GPa, which, according to the Monroe and Newman theory [23, 24], is more than enough to mechanically block the growth of lithium dendrite. However, recent experiments have revealed the opposite results [12 – 17]. Short-circuiting still occurs in ASSBs although the mechanisms could be fundamentally different from the dendritic growth observed in liquid electrolyte systems. In a polycrystalline ceramic SE, the short-circuits are usually associated with preferential deposition along the grain boundaries [18]. Single-crystal and amorphous SE are simply cracked with lithium deposition inside the cracks [19]. In spite of may experimental efforts to optimize SE or battery packs [20 – 22], it is still unclear why SE fail to inhibit lithium dendrites and how the cyclic performance of ASSBs can be improved. As experimental methods have the limitation in revealing all mechano-electrochemical details, such as stress distribution and evolution, theoretical analyses and numerical simulations are needed.

Researchers have taken various approaches to address the dendrite penetration problem. A seminal contribution in this area is the work of Monroe and Newman [23, 24]. They proposed an extended Butler-Volmer equation—incorporating the effects of the differences in hydrostatic and deviatoric stresses across the electrode-electrolyte interfaces as well as the surface tension of SE—to study the stability of interfaces between lithium and a polymeric

electrolyte. Their study led to the famous assertation that electrolytes with shear modulus twice that of lithium could stabilize the deposition process. However, in experiments lithium dendrites still grew [28 – 31] despite that the shear-modulus criterion is satisfied. Barai *et al*. [25, 26] proposed that a stable lithium deposition must induce compressive stresses in the electrode, electrolyte, and the newly deposited lithium metal; this requirement is however too stringent to achieve. Similarly, Ahmad and Viswanathan [27] proposed a perturbation solution of the equations governing the electrodeposition and stress development. In their model, heterogenous deposition is caused by the difference of the molar volumes of Li atoms (in electrode) and ions (in SE). Hence, they obtained a stability map based on the ratios of shear moduli and molar volume and argued that the existing SE are all in the unstable regimes because of the high shear modulus of inorganic SE and the increase in molar volume during electrodeposition. These theoretical works all indicate that the heterogenous deposition with inorganic SE is inevitable. In addition, actual electrode-electrolyte interfaces are non-smooth; asperity contacts cause cavities and protrusions which are also unavoidable initial defects [32]. It is then questionable whether dendrites can be inhibited after they nucleate.

In-situ observations have demonstrated cracks in inorganic SE and their propagation during lithium plating. Lithium dendrites then extended inside these cracks. For example, Porz *et al*. [33] conducted detailed experiments revealing cracks in a SE caused by charging, which is the main reason for short circuit. They developed a simplified one-dimensional chemo-mechanical model to calculate the stresses at a crack tip, which are functions of crack size and

Li-plating overpotential. However, Porz *et al*.'s model lacks rigorous mathematical treatment; it predicts very large stresses under a very small overpotential, which is probably unreliable (at least unvalidated). Klinsmann *et al*. [34] treated lithium in cracks as an incompressible, strengthless, and inviscid liquid. They found that the lithium metal inside SE cracks was pressurized very rapidly (reaching 1 GPa within seconds) during a normal charging process. Such a high pressure causes crack propagation, which continues until channels between two electrodes are formed, in which lithium dendrites extend to cause short circuit.

The growth of lithium dendrites in ASSBs is the consequence of multiphysics processes involving ion transport, electrochemical reaction, mechanical deformation, and crack propagation; hence, their coupling effects ought to be investigated. To unveil the impact of inherent mechanical and electronic properties of the grain boundary (GB) in polycrystalline SE on the Li penetration, Tantratian *et al*. [35] developed an electro-chemo-mechanical phase field model. Numerical results show that Li nucleates at the GB junctions on the Li-SE interface and propagates along the GB, at which the interfacial compressive stress is small due to the GB softening; moreover, the excess trapped electrons in the GB triggers an isolated Li nucleation in the bulk SE, which causes a self-amplified Li deposition until Li is interconnected to cause a short-circuit of ASSLBs. However, the cracking associated with the Li deposition is neglected. Assuming the cracked region is filled with Li throughout the process of dendrite penetration, the PF models proposed by Yuan *et al*. [36] to directly links the dendrite growth and crack propagation. They suggested that the high stiffness of a SE could

inhibit lithium dendrites but lead to high stress and high cracking tendency and that the large toughness could hinder crack propagation and mitigate dendrite growth. However, the mechano-electrochemical coupling (MEC) in electrodeposition was not considered in their model. Based on an analogy to stress corrosion cracking (SCC), Qi *et al*. [37] revealed that the dendrite penetration into SE is the consequence of the coupling of chemical reaction and local tensile stresses. Hence, they proposed that if compressive residual stresses in SE surfaces could inhibit dendrite penetration. However, a fully theoretical model to describe such a mechanism is still missing.

To have a deeper understanding of the MEC effect in dendrite penetration, we herein follow the above track of thought to establish a new theoretical model based on the phase-field (PF) method, in which the migration of lithium-SE interface is attributed to both mechanical cracking and lithium electrodeposition. Both cracking and electrodeposition are treated under a unified PF framework. The former is described in the form of the Allen–Cahn equation, consistent with the theory of strain energy release rate in fracture mechanics. The electrodeposition of lithium is described in the form of generalized Butler–Volmer (BV) equation wherein the MEC can be formulated. Incorporating further the Nernst–Planck–Poisson equation describing lithium-ion diffusion and the variation of electric field and a creep model describing the inelastic deformation of lithium, the model of lithium dendrite penetration in a SE is achieved. The prediction of the model is consistent with the established understandings, such as the inhibition effect of interfacial compressive stresses, which may

guide the multi-parametric optimization of ASSBs for eliminating or minimizing the risk of dendrite-induced short circuit. With the model, we ought to make clear the following issues: (1) how large are the stresses at the tips of lithium dendrite and SE crack, (2) how significant is the MEC effect, and (3) how to stabilize lithiation.

2. Methodology

Denoted by the order parameter ϕ the state of SE that contains defects and lithium deposit, we let $\phi = 1$ represent the cracks filled with lithium, $\phi = 0$ the defect-free SE, and $\phi \in (0, 1)$ the interfaces that migrate under electrochemical and mechanical forces. With the designation of the order parameter, we have made a simplification that a fully opened crack in SE is immediately filled with lithium metal. Though in reality cracks can propagate faster than lithium dendrite growth, our assumption in the present work is to simplify the formulation and foster the understanding of MEC effect during in ASSB. Such a simplification may be close the actual scenario when an ASSB is charged with very high current density, which is often employed in experimental studies. With the simplification, the governing equation of SE fracture and lithium deposition can be expressed as:

$$\frac{\partial \phi}{\partial t} = -L_{\text{int}}\left(W\frac{\partial g(\phi)}{\partial \phi} - \gamma_0 \delta_0 \left(\eta^2 \nabla^2 \phi - \frac{\partial}{\partial x}\left(\eta \frac{\partial \eta}{d\theta}\frac{\partial \phi}{\partial y} \right) + \frac{\partial}{\partial y}\left(\eta \frac{\partial \eta}{d\theta}\frac{\partial \phi}{\partial x} \right) \right) - \frac{\partial h(\phi)}{\partial \phi}\left(-\frac{\partial \psi^{\text{mech}}}{\partial \phi} \right) \right) + \frac{\partial h(\phi)}{\partial \phi} L_{\text{bulk}}\left(a_{\text{R}} \exp\left(\frac{(1-\alpha)\left(\mu_{\text{R}}^{\text{ex}} - \mu_{\text{P}}^{\text{ex}}\right)}{RT} \right) - a_{\text{P}} \exp\left(-\frac{\alpha\left(\mu_{\text{R}}^{\text{ex}} - \mu_{\text{P}}^{\text{ex}}\right)}{RT} \right) \right), \tag{1}$$

where the rate of interfacial migration, $\partial\phi/\partial t$, is governed by the two terms on the right-hand side of Eq. (1), representing the mechanical and electrodeposition forces. The first term describes cracking under mechanical loading, expressed in the form of the Allen–Cahn equation as derived in [38], which is consistent with the theory of strain energy release rate in fracture mechanics. Therein, L_{int} is interfacial mobility; $g(\phi) = \phi^2(1-\phi)^2$ is the double-well function to ensure that both defect and defect-free regions are stable; the pre-factor W is the energy barrier; $h(\phi) = \phi^3 (10 - 15\phi + 6\phi^2)$ is the interpolation function that varies from one to zero across the interface to mollify the effect of material discontinuity; $\partial h(\phi)/\partial\phi = 30\phi^2(1-\phi)^2$ is non-zero only in interfaces, hence ensuring that the fracture only occurs at interfaces; γ_0 and δ_0 are the Griffith energy density and interfacial thickness, respectively, ensuring that the Griffith criterion of brittle fracture is met in the PF model [38]; η is an orientation-dependent parameter to scale the anisotropy of Griffith energy density and thickness; θ is the angle between normal direction of interface and the nominal axis of system; ψ^{mech} is the elastic energy density.

The second term on the right-hand side of Eq. (1) is associated with the reaction kinetics of electrodeposition, thus expressed in the form of generalized BV equation. Therein, L_{bulk} is the coefficient to scale the contribution of electrodeposition kinetics to interface migration; $\alpha \in [0, 1]$ is the asymmetry parameter [39] to define the transition state in the electrochemical reaction; R and T are the ideal gas constant and thermodynamic temperature, respectively; a_{R} and a_{P} are the activities of reactants and products during electrodeposition reaction,

respectively; $\mu_{\mathrm{R}}^{\mathrm{ex}}$ and $\mu_{\mathrm{P}}^{\mathrm{ex}}$ are the excess chemical potentials of reactants and products, respectively. $\mu_{\mathrm{R}}^{\mathrm{ex}}-\mu_{\mathrm{P}}^{\mathrm{ex}}$ is the chemical potential difference during the electrodeposition, expressed as:

$$\begin{aligned}\mu_{\mathrm{R}}^{\mathrm{ex}}-\mu_{\mathrm{P}}^{\mathrm{ex}}=&\left(\mu_{\mathrm{Li}^{+},\mathrm{SE}}^{0}-\mu_{\mathrm{Li,S}}^{0}\right)+F\left(\varphi_{\mathrm{SE}}-\varphi_{\mathrm{S}}\right)+\\&\left[\frac{1}{c_{\mathrm{Li,S}}^{\mathrm{ref}}}h\left(\phi\right)\varepsilon^{\mathrm{eg}}\mathrm{tr}\left(\boldsymbol{\sigma}\right)-\left(1-h\left(\phi\right)\right)V_{a}\mathrm{tr}\left(\boldsymbol{\sigma}\right)+\frac{\partial h\left(\phi\right)}{2c_{\mathrm{Li,S}}^{\mathrm{ref}}\partial\phi}\left(\boldsymbol{\varepsilon}^{\mathrm{e}}\right)^{T}\left(\left(\mathbf{D}_{\mathrm{SE}}^{\mathrm{e}}-\mathbf{D}_{\mathrm{S}}^{\mathrm{e}}\right)\boldsymbol{\varepsilon}^{\mathrm{e}}\right)\right],\end{aligned}\tag{2}$$

where $\mu_{\mathrm{Li}^{+},\mathrm{SE}}^{0}$ and $\mu_{\mathrm{Li,S}}^{0}$ are the standard chemical potentials of lithium cations in SE and lithium atoms in deposit (S); F is the Faraday constant; φ_{SE} and φ_{S} are electrostatic potential in SE and deposit (S), respectively; $c_{\mathrm{Li,S}}^{\mathrm{ref}}$ is the reference concentration of lithium atom in deposit; $\varepsilon^{\mathrm{eg}}$ is the eigenstrain due to the volume expansion caused by lithium electrodeposition (i.e., the deposition onto the Li electrode is considered to be volume expansion); V_a is the partial mole volume change owing to stoichiometric expansion that results from the increasing fraction of diffusive lithium cation dissolved interstitially in the host lattice of SE; tr($\boldsymbol{\sigma}$) is the trace of the stress tensor; $\mathbf{D}_{\mathrm{SE}}^{\mathrm{e}}$ and $\mathbf{D}_{\mathrm{S}}^{\mathrm{e}}$ are the stiffness matrix of SE and lithium deposit, respectively; $\boldsymbol{\varepsilon}^{\mathrm{e}}$ is the elastic strain tensor. With Eq. (2), the reaction kinetics of electrodeposition depends not only on the instinct chemical potential difference, $\mu_{\mathrm{Li}^{+},\mathrm{SE}}^{0}-\mu_{\mathrm{Li,S}}^{0}$, and the applied electric potential difference, $\varphi_{\mathrm{SE}}-\varphi_{\mathrm{S}}$, but also on the stresses resulting from the eigenstrain in the process of lithium electrodeposition, $h\left(\phi\right)\varepsilon^{\mathrm{eg}}\mathrm{tr}\left(\boldsymbol{\sigma}\right)/c_{\mathrm{Li,S}}^{\mathrm{ref}}$, the stoichiometric expansion during the diffusion of lithium cations in SE, $\left(1-h\left(\phi\right)\right)V_{\mathrm{a,SE}}\mathrm{tr}\left(\boldsymbol{\sigma}\right)$, and the change in elastic properties during electrodeposition, $\left(\partial h\left(\phi\right)/\partial\phi\right)\left(\boldsymbol{\varepsilon}^{\mathrm{e}}\right)^{T}\left(\left(\mathbf{D}_{\mathrm{SE}}^{\mathrm{e}}-\mathbf{D}_{\mathrm{S}}^{\mathrm{e}}\right)\boldsymbol{\varepsilon}^{\mathrm{e}}\right)/\left(2c_{\mathrm{Li,S}}^{\mathrm{ref}}\right)$. It should be noted that such a stress-dependence is

not considered in previous models.

The governing equation of lithium diffusion can be expressed as:

$$\tau\frac{\partial\mu_{\mathrm{Li}}}{\partial t}=\nabla\left(\frac{D_{\mathrm{Li}}}{RT}\begin{pmatrix}h(\phi)c_{\mathrm{Li,S}}^{\mathrm{ref}}\exp\left(\dfrac{\mu_{\mathrm{Li}}-\mu_{\mathrm{Li,S}}^{0}}{RT}\right)+\\ \left(1-h(\phi)\right)c_{\mathrm{Li^{+},SE}}^{\mathrm{ref}}\exp\left(\dfrac{\mu_{\mathrm{Li}}-\mu_{\mathrm{Li^{+},SE}}^{0}}{RT}\right)\end{pmatrix}\left(\nabla\mu_{\mathrm{Li}}+F\nabla\varphi_{\mathrm{SE}}\right)\right),$$
$$-\frac{\partial h(\phi)}{\partial\phi}\left(c_{\mathrm{Li,S}}^{\mathrm{ref}}-c_{\mathrm{Li^{+},SE}}^{\mathrm{ref}}\right)\exp\left(\frac{\mu_{\mathrm{Li}}}{RT}\right)\frac{\partial\phi}{\partial t} \tag{3a}$$

$$\tau=\left(h(\phi)\frac{c_{\mathrm{Li,S}}^{\mathrm{ref}}}{RT}\exp\left(-\frac{\mu_{\mathrm{Li,S}}^{0}}{RT}\right)+\left(1-h(\phi)\right)\frac{c_{\mathrm{Li^{+},SE}}^{\mathrm{ref}}}{RT}\exp\left(-\frac{\mu_{\mathrm{Li^{+},SE}}^{0}}{RT}\right)\right)\exp\left(\frac{\mu_{\mathrm{Li}}}{RT}\right), \tag{3b}$$

where μ_{Li} is the chemical potential of lithium (in the interface and cracked region); $D_{\mathrm{Li}} = h(\phi)D_{\mathrm{S}} + (1-h(\phi))D_{\mathrm{SE}}$ is the diffusion coefficient of lithium species; and D_{S} and D_{SE} are the diffusion coefficients of lithium in the deposit and of Li cations in SE, respectively; $c_{\mathrm{Li,S}}^{\mathrm{ref}}$ and $c_{\mathrm{Li^{+},SE}}^{\mathrm{ref}}$ represent the reference (saturated) concentration of lithium in the deposit and Li cations in SE, respectively. On the right-hand side of Eq. (3a), the first term governs the diffusion of lithium species due to concentration gradient and electropotential field, and the second term governs the consumption rate of Li cations due to electrodeposition.

The Poisson's equation is employed to determine the electropotential field, φ, given by:

$$\nabla\left(\varepsilon\nabla\varphi\right)=Fc_{\mathrm{Li,S}}^{\mathrm{ref}}\frac{\partial\phi}{\partial t}, \tag{4}$$

where ε is the effective electric conductivity of the medium, given by $\varepsilon = \varepsilon_{\mathrm{S}}h(\phi) + \varepsilon_{\mathrm{SE}}(1 - h(\phi))$ with ε_{S} and ε_{L} being the conductivities of the deposit and SE, respectively; and the right-hand side, $Fc_{\mathrm{Li,S}}^{\mathrm{ref}}\left(\partial\phi/\partial t\right)$, represent the change rate of charge density due to the supply of electrons

during electrodeposition. All governing equations as above-mentioned are also listed in Table 1.

Table 1

It is note that in present model, the SE is considered to be defect-free and grain boundary free, such as the single crystal LLZTO. Thus, the influence of defect and grain boundary on the lithium penetration is ignore. The detailed derivation of the present PF model with the Ref. [26, 40 – 46] is described in the Supplementary information.

3. Numerical results and discussion

In present section, the numerical simulations are presented: firstly, a typical lithium dendrite penetration in brittle SE is modeled to reveal why the relative softer lithium dendrite can quicky 'pierce' the much harder SE and cause unexpected short circuit; secondly, effect of mechanical-electrochemical coupling (MEC) on the lithium penetration in SE is investigated; finally, by considering the effects of MEC, the properties of SE (involving the Youngs modulus, the fracture toughness), as well as the applied stress, the suppression strategies are present to inhibit the lithium penetration in SE. The detailed boundary conditions and materials parameters with the Ref. [23, 27, 35, 36, 42, 43, 48] are described in the Supplementary information.

3.1. Results of lithium dendrite penetration in brittle SE

Fig. 1

To demonstrate results of the PF model, we consider a two-dimensional simulation

domain with the top boundary being the symmetric axis of a dendrite and the bottom boundary representing a far field. The simulation results of the numerical model are shown in Fig. 1, in which, the applied voltage (φ_{apply}), the Youngs modulus of SE (E_{SE}), and the volumetric eigenstrain (ε^{eg}) are 75 mV, 175 GPa, and 0.008, respectively. In the results shown in Fig. 1, the MEC (in Eq. (2)) is ignored. Fig. 1(a) shows a typical heterogeneous deposition, i.e., the initial semi-circle hump grows quickly into a needle-like dendrite while the bottom interface moves slowly and remains flat. Furthermore, by tracking the position of the dendrite tip and the bottom interface in x direction, the heterogeneous deposition is quantitatively studied in Fig 1(b), which shows an accelerated lengthening of dendrite tip and a decelerated movement of the interface (originally flat) next to the dendrite. Such a heterogeneous Li deposition can be attributed to the localized nonuniform electrochemical environment and the cracking of SE.

The variations of electropotential and Li cation concentration in SE are shown in Figs. 1(c) and (d), respectively, which are more and more inhomogeneous during deposition. The distributions of electropotential along the top (passing dendrite tip) and bottom (flat interface) boundaries of the numerical model are plotted in Fig. 1(e), exhibiting an increase in the electropotential gradient near the dendrite tip and a decrease near the bottom interface. Similarly, the inhomogeneous distributions of lithium cation concentration are shown in Fig. 1(f). It is noted that the concentration gradient is almost unchanged near the tip while decreases with time near the bottom interface. With such inhomogeneous electric and concentration fields, the overpotential increases near the dendrite tip and decreases near the bottom interface,

driving the transport of lithium cations from the far field to the tip rather than the bottom, i.e., the dendritic growth is promoted.

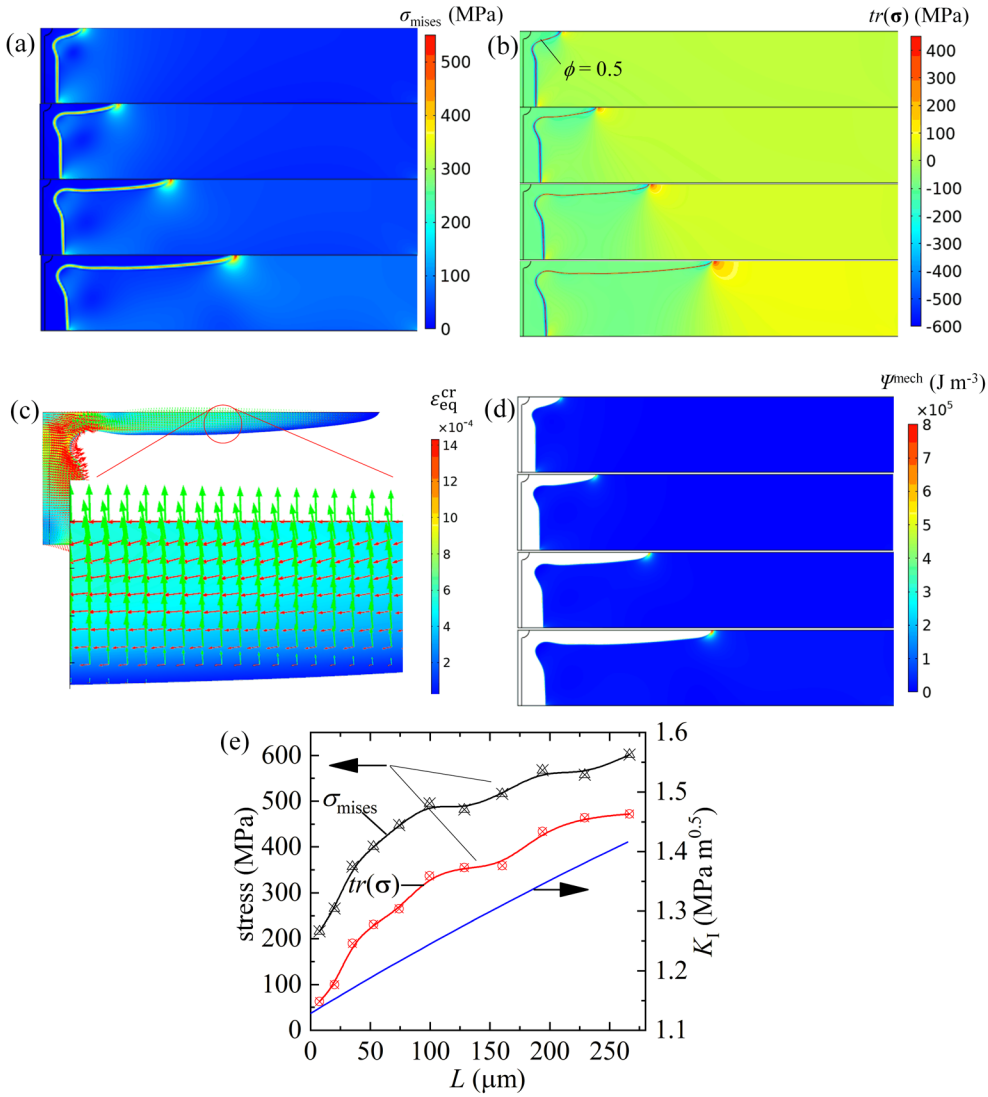

Fig. 2 Contour plots of (a) the mises stress, σ_{mises}, (b) the trace of stress tensor, $tr(\sigma)$, (c) the equivalent creep strain, ε_{eq}^{cr}, and (d) the elastic energy density, ψ^{mech}, respectively; (e) the variations of σ_{mises}, $tr(\sigma)$ and the stress-intensity factor, K_I in SE next to the dendrite tip with the length of lithium dendrite, L.

Different from lithium dendrites in liquid electrolyte, the dendrite growth in an ASSB is associated with SE cracking that provides room for lithium dendrites to pierce. SE cracking is a mechanical process induced by a dilatative stress state as the result of lithium intrusion. Figs. 2(a) and (b) shows the evolution of the Von Mises stress, σ_{mises}, and the trace of stress tensor, $tr(\boldsymbol{\sigma})$, during deposition, respectively. It is observed that the stress in lithium is almost isotropic, i.e., the deviatoric stress measure (σ_{mises}) is only 1% of the hydrostatic pressure. The reasons are that the stress in lithium is due to the squeeze of surrounding SE and the room-temperature creep of lithium furtherly relaxes deviatoric stress components. As shown in Fig. 2(c), the equivalent creep strain, $\varepsilon_{\text{eq}}^{\text{cr}}$, creep strain is remarkable which quickly relaxes the deviatoric stress components leading to a small Von Mises stress. It is also note that different from the view of LePage *et al*. [43] that there is creep flow with a boundary layer away from the dendrite tip, in present simulation, the creep strain can be divided into two components: one is along the dendrite away from the tip and the other is normal to the dendrite boundary and towards the inside of dendrite. It is because, in the view of LePage *et al*. [43], the lithium dendrite is treated as an incompressible, strengthless, and viscid liquid, thus the creep deformation likes an incompressible viscous fluid flow which is along the crack boundary.

The deposition of lithium at the dendrite tip leads to the tensile stress in SE near the tip. Note that it is different from the 1D theorical results described in Ref. [23 – 27], in which the stress in SE is compressive rather than tensile. With the dendrite growth, such a tensile stress concentration becomes increasingly significant, and the strain energy stored near the tip (Fig.

2(d) can be larger than the energy required to generate new surfaces of SE (i.e., the Griffith criterion); hence, cracking in SE takes place. The progress of dendrite penetration in brittle SE is similar to a mode-I cracking process, in which the fracture toughness of SE, K_{IC}, rather than the shear modulus [23, 24], is the dominant factor. In Fig. 2(e), the blue curve shows the stress-intensity factor for a mode-I crack (expressed in Eq. (S31) in Supplementary information), K_I, with the length of dendrite. The magnitude of initial K_I is about 1.4 MPa $m^{0.5}$, larger than the SE's fracture toughness of K_{IC} = 1.07 MPa $m^{0.5}$ (calculated by following Yuan *et al*. [36], as expressed in Eq. (S32) in Supplementary information) and that K_I increases at an accelerated rate, leading to an expedited crack propagation.

In our model, the volumetric eigenstrain, ε_m^{eg}, is the key factor in describing the effect of lithium precipitation from SE. The increases in ε_m^{eg} leads to the more significant increase in stresses in lithium and SE. To exemplify, we changed ε_m^{eg} from 0.008 to 0.012 and demonstrate the increases in the maximum Mises stress, σ_{mises}, and the trace of stress tensor, $tr(\boldsymbol{\sigma})$ at the crack tip of SE in Fig. 3(a, b). Such a stress concentration leads to a very rapid increase in K_I, as shown in Fig. 3(c). For example, when ε_m^{eg} = 0.012, the stress-intensity factor, K_I, increases from 1.4 to 2.7 MPa $m^{0.5}$ with the length of lithium dendrite. It leads to a quick lengthening of lithium dendrite from 0 to about 500 μm as shown in Fig. 3(d). This is the reason why the relative softer lithium dendrite can quicky 'pierce' the much harder SE and cause unexpected short circuit.

Fig. 3

The initial nucleation radius of deposited Li also has the impacts on the growth of Li dendrite in SE. It is observed that the maximum length of Li dendrite after 200 s decreases with the increase of initial nucleation radius r (see Fig. 4(a)). It is because the increase in the initial nucleation radius leads to the increase in the surface area participating the electrodeposition reaction that results in the increase in the average reaction rate near the nucleate site while the decrease in the maximum reaction rate at the tip of nucleate site. Consequently, the larger initial nucleation radius leads to a shorter but thicker Li dendrite with a blunter tip, that results in the decrease in the stress concentrated in SE near the tip of dendrite. Thus, the decrease in the mean stress-intensity factor, $K_{\mathrm{I,\,m}}$, with r is also observed in Fig. 4(b). It is also note that since the larger initial nucleation radius results in a larger stress near in SE, the initial stress-intensity factor increases with the increase in r (see the insert map of Fig. 4(b)).

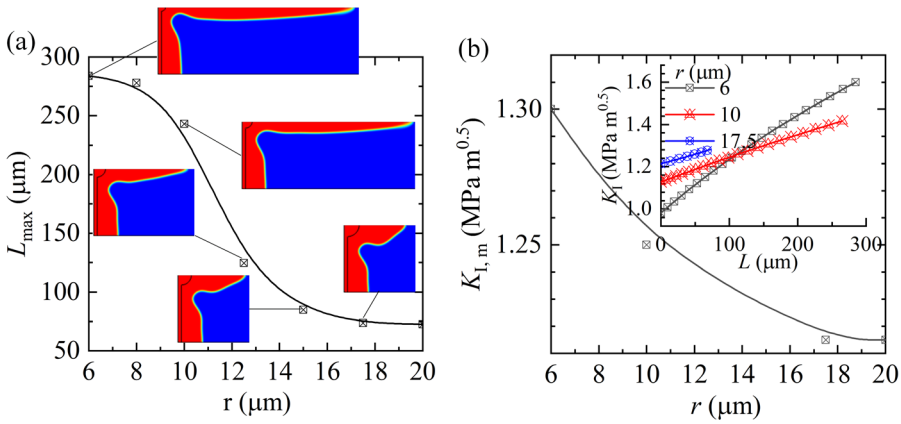

Fig. 4 Evolution of (a) maximum length of Li dendrite after 200 s and (b) the mean stress-intensity factor, $K_{\mathrm{I,\,m}}$, with the increase of initial nucleation radius r.

3.2. The effect of MEC on lithium penetration in SE

The MEC may be assessed by assuming that the hydrostatic compressive stress in lithium reduces the overpotential, as expressed in Eq. (2), which suppresses the reaction kinetics. Fig. 5(a) shows the reduction in overpotential when MEC is turned on in our numerical model with $\varphi_{apply} = 75$ mV, $E_{SE} = 175$ GPa, and $\varepsilon_m^{eg} = 0.008$. With the MEC, the reduction in overpotential is almost a constant (~ -2.4 mV) during lithium dendrite lengthening and the stress-intensity factor, K_I, is also debased, as shown in Fig. 5(b). The difference in K_I with and without MEC increases during the lengthening of lithium dendrite. Consequently, MEC reduces electrochemical reaction and the strain energy release rates, leading to a slower dendrite penetration in SE.

Fig. 5

With MEC, the increase in the volumetric eigenstrain leads to the more remarkable decrease in the overpotential and slows down the electrochemical reaction kinetics. On the other hand, it causes the increase in K_I that accelerates cracking. As shown in Fig. 6(a), considering MEC, the increase in ε_m^{eg} from 0.008 to 0.012 leads to the average shift in overpotential, $\Delta\varphi_m$, from -2 to -5 mV and the increase in mean stress-intensity factor, $K_{I,m}$, from 1.3 to 1.9 MPa $m^{0.5}$, respectively. While for the uncoupled scenario, the mean stress-intensity factor, $K_{I,m}$, increases from 1.4 to 2.0 MPa $m^{0.5}$. Fig. 6(b) shows the increase in the maximum length of lithium dendrite, L_{max}, with ε_m^{eg}. It is noted that the difference of L_{max} between the uncoupled and coupled scenarios increases with ε_m^{eg}, as shown in Fig. 6(b).

Fig. 6

Because the growth of lithium dendrite in ASSB is also related to the mechanical property of SE, we vary both E_{SE} and ε_m^{eg} to study their influences. Fig. 6(c) shows the evolution of $\Delta\varphi_m$ and $K_{I,m}$ with E_{SE} and ε_m^{eg}. In this scenario, $\Delta\varphi_m$ is nearly unchanged with E_{SE}, which indicates that the hydrostatic pressure in lithium is insensitive to the variation of mechanical properties of SE. While $K_{I,m}$ increases with the increase of E_{SE} due to the increase in stresses in SE, indicating that stiffer SE does not suppress but promotes the dendrite penetration. In Fig, 5(d), we exemplify the increase in the length of lithium dendrite at 200s, L_{max}, with the increase in ε_m^{eg} and E_{SE}.

If we consider the stoichiometric expansion, V_a, resulting from the increase in the concentration of Li cations dissolved interstitially in the host lattice of SE, the stresses in SE also have the effect on the electrochemical reaction kinetics. As expressed in Eq. (2), compressive stresses in lithium deposition cause the decrease in the overpotential, while in SE tensile stresses result in the decrease in the overpotential because SE lattice under tension can be more accommodative to lithium cations. Fig. 7(a) shows the variations of $\Delta\varphi$ and K_I with L. It is observed that when V_a increases from 0.5 to 6 $cm^3\ mol^{-1}$, the overpotential shift, $\Delta\varphi$, at the tip of dendrite significantly increase from -5 to -35 mV. The increase in V_a also results in a blunter dendrite tip as shown in Fig. 7(a) and a remarkable decrease in K_I. When $V_a = 6\ cm^3\ mol^{-1}$, a significant suppression in the growth of lithium dendrite in ASSB is observed, as shown in Fig. 7(b).

Fig. 7

Fig. 7(c) shows the decreases in $\Delta\varphi_m$ and $K_{I,m}$ with V_a, indicating that the increase in V_a slows down the electrochemical reaction and strain energy release at the tip of dendrite; hence, the length of lithium dendrite, L_{max}, is reduced with V_a, as shown in Fig. 7(d). Note that this result is different from the theoretical studies by Barai *et al*. [25, 26] and Ahmad and Viswanathan [27]. In their studies, the increase in V_a promotes the electrochemical reaction because the stress in SE is compressive rather than tensile due to the assumption of flat-interface. The increase in E_{SE} results in the increase in the tensile stress in SE at the tip of lithium dendrite, leading to the further decrease in the overpotential (the black and red lines in Fig. 7(e)) that suppresses the deposition. Concomitantly, it causes the increase in K_I as shown in Fig. 7(e), which promotes the cracking. With the increase in V_a, the decrease in the overpotential is more significant than the decrease in K_I . L_{max} increases with E_{SE} and reduces with V_a. With a very significant V_a, the competition of the effects of E_{SE} can leads to a nonmonotonic change in L_{max}, because the tension-induced suppression in the overpotential can overtake the promotion in K_I. As shown in Fig. 7(f), when $V_a = 6$ cm^3 mol^{-1}, L_{max} decreases from 160 to 140 μm when E_{SE} increases from 50 to 100 GPa, which provides a window to mitigate dendrite penetration.

3.3. Suppression strategies to inhibit the dendrite penetration in SE

Fig. 8

As above mentioned, the dendrite penetration in SE is attributed mainly to the brittleness

of SE. Accordingly, the dendrite penetration can be suppressed by the increase of the fracture toughness of SE. According to Eq. (S32), the fracture toughness of SE can be increased by either the increase in the surface energy density required to create new fracture surface, γ, or the Young's module of SE, E_{SE}. Fig. 8(a) shows a precipitous drop in the mean stress-intensity factor, $K_{I,\,m}$, with the increase in γ, indicating that cracking in SE can be effectively suppressed by increasing the surface energy density of SE. When γ is larger than 3.5 J m^{-2}, the mean stress-intensity factor, $K_{I,\,m}$, becomes smaller than the fracture toughness of SE, K_{IC}; hence a stable lithium deposition is achieved as shown in Fig. 8(b), that is the lithium dendrite does not penetrate into the SE. Fig. 8(c) shows the increase in $K_{I,\,m}$ with E_{SE}. If the surface energy density is sufficiently large (i.e., γ > 3.5 J m^{-2}), the fracture toughness of SE, K_{IC}, becomes increasingly larger than the mean stress-intensity factor, $K_{I,\,m}$ with the increase in E_{SE}; in this case, the increase in the Young's module of SE can suppress dendrite penetration in ASSB, as shown in Fig. 8(d). However, if γ < 3.5 J m^{-2}, cracking and lithium dendrite penetration becomes increasingly severe with E_{SE}, manifested by the increase in L_{max} with E_{SE}.

Fig. 9

As suggested by Qi *et al*. [37], if the SE surface against lithium is under compressive residual stresses, it is expected that the dendrite penetration in the SE can be inhibited. Hence, a surface compressive traction, F_a, normal to the direction of dendrite growth is applied to SE to evaluate its influence. Fig. 9(a) shows that the variation of $tr(\boldsymbol{\sigma})$ at the tip of dendrite with F_a. During the lengthening of lithium dendrite, $tr(\boldsymbol{\sigma})$ decreases from about 1000 to 400 MPa

when F_a increases from 0 to 100 MPa. Such a decrease in $tr(\boldsymbol{\sigma})$ causes the decrease in K_{I}. As shown in Fig. 9(b), when the applied traction is sufficiently large ($F_a \geq 50$ MPa), the decrease rather than increase in K_{I} with dendrite lengthening results. Such a decrease in $tr(\boldsymbol{\sigma})$ can results in the decrease in the shift of overpotential that promotes the electrochemical reaction (see Fig. 9(c)). Fig. 9(d) shows the variations of mean stress-intensity factor, $K_{\mathrm{I,\,m}}$, and the mean overpotential shift, $\Delta\varphi_{\mathrm{m}}$, with F_a. It is observed that with the increase in F_a, the decrease in $K_{\mathrm{I,\,m}}$ is very significant while the decrease of overpotential is mild, indicating that the applied traction can inhibit dendrite growth (see Fig. 9(d)). Specifically, if F_a is larger than 100 MPa, the mean stress-intensity factor, $K_{\mathrm{I,\,m}}$, becomes smaller than the facture toughness of SE, K_{IC}; hence, cracking in SE can be stopped.

It is note that, since the lithium growth in SE is attributed to both the cracking and the heterogenies electrodeposition reaction. The applied in-plane compression can merely inhibit the cracking, while it does not have a material impact on the deposition reaction. Thus, once the cracking is completely inhibited, the further increase in applied compression is no longer benefit for dendrite suppression as shown in Fig. 9(e). In this case dendrite growth is completely attributed to the heterogenies lithium electrodeposition. That is why some experimental findings show that the length of dendrite dose not decrease infinitely with the increase of applied stress [49].

4. Concluding remarks

A new PF model is proposed to study the mechanism of lithium dendrite penetration in ASSBs. The reaction-diffusion kinetics, nonuniform electric and stress fields, and cracking are described. The numerical results reveal how the dendrite penetration into a SE is induced by lithium deposition. With the simulations and parametric studies, we achieved the following concluding remarks.

(1) Lithium deposition can be treated as a volume expansion delineated by a volumetric eigenstrain. Under confinement and considering the creep of lithium, the deposition process leads to hydrostatic pressure in lithium and tensile stresses concentrated at a crack tip in SE. The latter leads to Mode-I cracking in SE and dendrite penetration. Hence, the fracture toughness of SE, K_{IC}, is the more important property than the shear modulus emphasized by Monroe *et al*. [23, 24] to enhance.

(2) Considering MEC, the hydrostatic pressure in lithium may suppress the reaction kinetics, manifested by the shift of overpotential. Thus, the dendrite penetration may be delayed; however, it cannot be avoided. We further involved the volumetric eigenstrain in SE due to the concentration of interstitial lithium ions and assumed that tensile stresses in SE can also reduce the overpotential, it leads to the possibility that a very stiff SE may suppress dendrite penetration.

(3) Toughening SE, e.g., a SE with high surface energy, γ, is an effective strategy in suppressing dendrite penetration. With a sufficiently large γ, increasing the Young's modulus of SE leads

the better suppression of lithium dendrites, as it leads to an increase in toughness. As the existing SE have limited toughness, inducing compressive Li-SE interfaces, e.g., through the engineering residual stresses, has been suggested as a more realistic strategy to suppress dendrites. In this case, the dendrite penetration in SE can be significantly inhibited when F_a increases from 0 to 100 MPa.

Data Availability

The data that support the findings of this study are available from the corresponding author upon reasonable request.

Acknowledgments

C. L. acknowledges the support from Natural Science Foundation of Guangdong Province (2022A1515011891) and Guangdong Major Project of Basic and Applied Basic Research (2019B030302011). H. H. R. acknowledges the support of the General Research Fund of the Hong Kong Research Grants Council (Grant No.: 15213619, Account code: Q73H).

Author Contribution

C. L. and H. H. R. conceived the idea; C. L. was responsible for model establishment; C.L. and L.X. conducted simulations; C. L. and H. H. R. analyzed the results and wrote the manuscript.

Additional Information

Competing Interest: The authors declare no competing interests.

References

[1] A. Manthiram, An Outlook on Lithium Ion Battery Technology, ACS Cent. Sci. 3 (2017) 1063−1069.

[2] https://www.energy.gov/eere/solar/articles/solar-plus-storage-101.

[3] J. Li, D. Sun, X. Jin, W. Shi, C. Sun, Lithium-ion battery overcharging thermal characteristics analysis and an impedance-based electro-thermal coupled model simulation, Appl. Energy 254 (2019) 113574.

[4] J. Lamb, C.J. Orendorff, K. Amine, G. Krumdick, Z. Zhang, L. Zhang, A.S. Gozdz, Thermal and overcharge abuse analysis of a redox shuttle for overcharge protection of LiFePO 4, J. Power Sources 247 (2014) 1011–1017.

[5] J. Lamb, C.J. Orendorff, L.A.M. Steele, S.W. Spangler, Failure propagation in multi-cell lithium ion batteries, J. Power Sources 283 (2015) 517–523.

[6] Z. Liao, S. Zhang, K. Li, G. Zhang, T.G. Habetler, A survey of methods for monitoring and detecting thermal runaway of lithium-ion batteries, J. Power Sources 436 (2019) 226879.

[7] S. Arora, W. Shen, A. Kapoor, Review of mechanical design and strategic placement technique of a robust battery pack for electric vehicles, Renew. Sust. Energ. Rev. 60 (2016) 1319–1331.

[8] Q. Liu, X. Su, D. Lei, et al., Approaching the capacity limit of lithium cobalt oxide in lithium ion batteries via lanthanum and aluminium doping, Nat. Energy 3 (11) (2018) 936–943.

[9] J. Li, C. Ma, M. Chi, C. Liang, N.J. Dudney, Solid electrolyte: the key for high-voltage lithium batteries, Adv. Energy Mater. 5 (2015) 1401408.

[10] Y. Zhu, X. He, Y. Mo, Origin of outstanding stability in the lithium solid electrolyte materials: insights from thermodynamic analyses based on first-principles calculations, ACS Appl. Mater. Interfaces 7 (42) (2015) 23685.

[11] W.D. Richards, L.J. Miara, Y. Wang, J.C. Kim, G. Ceder, Interface stability in solid-state batteries, Chem. Mater. 28 (1) (2015) 266.

[12] H.-D. Lim, J.-H. Park, H.-J. Shin, J. Jeong, J.T. Kim, K.-W. Nam, H.-G. Jung, K. Y. Chung, A review of challenges and issues concerning interfaces for all-solid-state batteries, Energy Storage Mater. 25 (2020) 224–250.

[13] E.J. Cheng, A. Sharafi, J. Sakamoto, Intergranular Li metal propagation through polycrystalline Li6.25Al0.25La3Zr2O12 ceramic electrolyte, Electrochim. Acta 223 (2017) 85–91.

[14] R. Hongahally Basappa, T. Ito, T. Morimura, R. Bekarevich, K. Mitsuishi, H. Yamada, Grain boundary modification to suppress lithium penetration through garnet-type solid electrolyte, J. Power Sources 363 (2017) 145–152.

[15] J.A. Lewis, J. Tippens, F.J.Q. Cortes, M.T. McDowell, Chemo-mechanical challenges in solid-state batteries, Trends Chem. 1 (2019) 845–857.

[16] M. Nagao, A. Hayashi, M. Tatsumisago, T. Kanetsuku, T. Tsuda, S. Kuwabata, In situ SEM study of a lithium deposition and dissolution mechanism in a bulk-type solid-state cell with a Li2S–P2S5 solid electrolyte, Phys. Chem. Chem. Phys. 15 (2013) 18600–18606.

[17] K. Kerman, A. Luntz, V. Viswanathan, Y.-M. Chiang, Z. Chen, Review—practical challenges hindering the development of solid state Li Ion batteries, J. Electrochem. Soc. 164 (2017) A1731–A1744.

[18] E. J. Cheng, A. Sharafi, and J. Sakamoto, Intergranular Li metal propagation through polycrystalline Li6.25Al0.25La3 Zr2O12 ceramic electrolyte, Electrochimica Acta 223 (2017) 85–91.

[19] T. Swamy, R. Park, B. W. Sheldon, D. Rettenwander, L. Porz, S. Berendts, R. Uecker, W. C. Carter, and Y. M. Chiang, Lithium metal penetration induced by electrodeposition through solid electrolytes: example in single-crystal Li6La3ZrTaO12 garnet, J. Electrochem. Soc. 165 (2018) A3648.

[20] J. Chen, J.W. Wu, X.D. Wang, A.A. Zhou, Z.L. Yang, Research progress and application prospect of solid-state electrolytes in commercial lithium-ion power batteries, Energy Storage Mater. 35 (2021) 70–87.

[21] Y.Y. Sun, F. Li, P.Y. Hou, Research progress on the interfaces of solid-state lithium metal batteries, J. Mater. Chem. A 9 (2021) 9481–9505.

[22] Q. Lv, Y.P. Jiang, B. Wang, Y.J. Chen, F. Jin, B.C. Wu, H.Z. Ren, N. Zhang, R.Y. Xu, Y.H. Li T.R. Zhang, Y. Zhou, D.L. Wang, H.K. Liu, S.X. Dou, Suppressing lithium dendrites within inorganic solid-state electrolytes, Cell Rep. Phys. Sci. 3 (2022) 100706.

[23] C. Monroe, J. Newman, The effect of interfacial deformation on electrodeposition kinetics, J. Electrochem. Soc. 151 (2004) A880–A886.

[24] C. Monroe, J. Newman, The impact of elastic deformation on deposition kinetics at lithium/polymer interfaces. J. Electrochem. Soc. 152 (2005) A396–A404.

[25] P. Barai, K. Higa, V. Srinivasan, Lithium dendrite growth mechanisms in polymer electrolytes and prevention strategies. Phys. Chem. Chem. Phys. 19 (2017) 20493–20505.

[26] P. Barai, A.T. Ngo, B. Narayanan, K. Higa, L.A. Curtiss, V. Srinivasan, The role of local inhomogeneities on dendrite growth in LLZO-based solid electrolytes. J. Electrochem. Soc. 167 (2020) 100537.

[27] Z. Ahmad, V. Viswanathan, Stability of Electrodeposition at Solid-Solid Interfaces and Implications for Metal Anodes, Phys. Rev. Lett. 119 (2017) 056003.

[28] Y. Ren, Y. Shen, Y. Lin, C.W. Nan, Direct observation of lithium dendrites inside garnet-type lithium-ion solid electrolyte, Electrochem Commun 57 (2015) 27–30.

[29] A. Sharafi, H.M. Meyer, J. Nanda, J. Wolfenstine, J. Sakamoto, Characterizing the Li-Li7La3Zr2O12 interface stability and kinetics as a function of temperature and current density, J Power Sources 302 (2016) 135–139.

[30] E. Cheng, A. Sharafi, J. Sakamoto, Intergranular Li metal propagation through polycrystalline Li6.25Al0.25- La3Zr2O12 ceramic electrolyte, Electrochim Acta 223 (2016) 85–91.

[31] F. Aguesse, W. Manalastas, L. Buannic, J.M. Lopez del Amo, G. Singh, A. Llords, J. Kilner, Investigating the dendritic growth during full cell cycling of garnet electrolyte in direct contact with li Metal, ACS Appl Mater Interfaces 9 (2017) 3808–3816.

[32] Z.Y. Ning, D.S. Jolly, G.C. Li, R.D. Meyere, S.D. Pu, Y. Chen, J. Kasemchainan, J. Ihli, C. Gong, B. Liu, D.L.R. Melvin, A. Bonnin, O. Magdysyuk, P. Adamson, G.O. Hartley, C.W. Monroe, T.J. Marrow, P.G. Bruce, Visualizing plating-induced cracking in lithium-anode solid-electrolyte cells, Nat. Mater. 20(2021), 1121–1129.

[33] L. Porz, T. Swamy, B.W. Sheldon, D. Rettenwander, T. Frmling, H.L. Thaman, S. Berendts, R. Uecker, W.C. Carter, Y.M. Chiang, Mechanism of lithium metal penetration through inorganic solid electrolytes, Adv Energy Mater 7 (2017) 1701003.

[34] M. Klinsmann, F.E. Hildebrand, M. Ganser, R.M. McMeeking, Dendritic cracking in solid electrolytes driven by lithium insertion, J Power Sources 442 (2019) 227226.

[35] K. Tantratian, H.H. Yan, K. Ellwood, E.T. Harrison, L. Chen, Unraveling the Li Penetration Mechanism in Polycrystalline Solid Electrolytes, Adv. Energy Mater. 11 (2021) 2003417.

[36] C.H. Yuan, W.Q. Lu, J. Xu, Unlocking the Electrochemical–Mechanical Coupling Behaviors of Dendrite Growth and Crack Propagation in All-Solid-State Batteries, Adv Energy Mater (2021) 2101807.

[37] Y.Qi, C.M. Ban, S. J. Harris, A New General Paradigm for Understanding and Preventing Li Metal Penetration through Solid Electrolytes, Joule 4 (2020) 1–10.

[38] P. J. Loew, B. Peters, L.A.A. Beex, Rate-dependent phase-field damage modeling of rubber and its experimental parameter identification, J Mech. Phys. Solids 127 (2019) 266–294.

[39] A.M. Kuznetsov, J. Ulstrup, Electron Transfer in Chemistry and Biology: An Introduction to the Theory, Wiley: Chichester, U.K. (1999).

[40] T.-T. Nguyen, J. Yvonnet, M. Bornert, C. Chateau, K. Sab, R. Romani, R.L. Roy, On the choice of parameters in the phase field method for simulating crack initiation with experimental validation, Int. J. Fract. 197 (2016) 213–226.

[41] J.M. Debierre, A. Karma, F. Celestini, R. Guerin, Phase-field approach for faceted solidification, Phys. Rev. E, 68 (2003) 041604.

[42] Z.H. Fu, X. Chen, C.Z. Zhao, H. Yuan, R. Zhang, X. Shen, X.X. Ma, Y. Lu, Q.B. Liu, L.Z. Fan, and Q. Zhang, Stress Regulation on Atomic Bonding and Ionic Diffusivity: Mechanochemical Effects in Sulfide Solid Electrolytes, Energy Fuels 35 (2021) 10210–10218.

[43] W.S. LePage, Y.X. Chen, E. Kazyak, K.H. Chen, A.J. Sanchez, A. Poli, E.M. Arruda, M. D. Thouless, N.P. Dasgupta, Lithium Mechanics: Roles of Strain Rate and Temperature and Implications for Lithium Metal Batteries, J. Elec. Soc. 166 (2019) A89–A97.

[44] M.Z. Bazant, Theory of chemical kinetics and charge transfer based on nonequilibrium thermodynamics, Acc Chem. Res., 46 (2013) 1144–1160.

[45] F. C. Larche, J. L. Cahn, The effect of self-stress on diffusion in solids, Acta Metall., 30 (1982) 1835–1845.

[46] S. G. Kim, W. T. Kim, and T. Suzuki, Phase-field model for binary alloys, Phys. Rev. E, 60 (1999) 7186.

[47] G. V. Samsonov, Handbook of the Physicochemical Properties of the Elements, New York 1968.

[48] L. Chen, H.W. Zhang, L.Y. Liang, Z. Liu, Y. Qi, P. Lu, J. Chen, L. Chen, Modulation ofdendritic patterns during electrodeposition: a nonlinear phase-field model, J. Power Sources 300 (2015) 376–385.

[49] C. Fang, B. Lu, G. Pawar, M. Zhang, D. Cheng, S. Chen, M. Ceja, J. Doux, H. Musrock, Mei Cai, B. Liaw, Y. Meng, Pressure-tailored lithium deposition and dissolution in lithium metal batteries, Nature Energy 6 (2021) 987–994.

Figure caption

Fig. 1. Typical numerical results obtained under an applied voltage of φ_{apply} = 75 mV and the SE's Youngs module of E_{SE} = 175 GPa; (a, c, d) contour plots of order parameter, electric field and lithium cation concentration, respectively; (b, e, f) movements of interfaces, distributions of electropotential, and lithium cation concentration, respectively, along the top (passing dendrite tip) and bottom (flat interface) boundaries of the numerical model.

Fig. 2. Contour plots of (a) the mises stress, σ_{mises}, (b) the trace of stress tensor, $tr(\boldsymbol{\sigma})$, and (c) the elastic energy density, ψ^{mech}, respectively; (d) the variations of σ_{mises}, $tr(\boldsymbol{\sigma})$ and the stress-intensity factor, K_I in SE next to the dendrite tip with the length of lithium dendrite, L.

Fig. 3. The effect of eigenstrain, ε_m^{eg} = 0.008–0.012: (a, b, c) evolutions of mises stress, σ_{mises}, trace of stress tensor, $tr(\boldsymbol{\sigma})$, and stress-intensity factor, K_I, with the length of lithium dendrite, L, respectively, and (d) the variation of L with time. In the simulation E_{se} = 175 GPa and φ_{apply} = 75 mV.

Fig. 4. Evolution of (a) maximum length of Li dendrite after 200 s and (b) the mean stress-intensity factor, $K_{I,m}$, with the increase of initial nucleation radius r.

Fig. 5. Effects of MEC: (a, b) variations of overpotential shift, $\Delta\varphi$, and stress intensity factor, K_I, with dendrite length, L, and contour plots of $\Delta\varphi$, respectively, and (b) variations of the dendrite length, L, with time.

Fig. 6. MEC Effects against changes in E_{SE} (50 – 175 GPa) and ε_m^{eg} (0.008 – 0.012): (a) variations of the mean overpotential shift, $\Delta\varphi_m$, and the mean stress-intensity factor, $K_{I,m}$ with

ε_m^{eg}, (b) the variation of dendrite length at 200 s, L_{max}, with ε_m^{eg}, (c) variations of $\Delta\varphi_m$ and $K_{I,m}$ with E_{SE} for different magnitudes of ε_m^{eg} and (d) the evolution of L_{max} with ε_m^{eg} and E_{SE}.

Fig. 7. Variations of (a) the overpotential shift, $\Delta\varphi$ and the stress-intensity factor, K_I, with the length of lithium dendrite, L, (b) the length of lithium dendrite, L, with time for different V_a; and effects of stoichiometric expansion, V_a (0.5 – 6 $cm^3\ mol^{-1}$): variations of (c) the mean overpotential shift, $\Delta\varphi_m$, and mean stress-intensity factor, $K_{I,m}$, and (d) the largest length of lithium dendrite, L_{max}, with V_a for E_{SE} = 175 GPa, and variations of (e) $\Delta\varphi_m$ and $K_{I,m}$ and (f) L_{max} with E_{SE} for different values of V_a.

Fig. 8. Variations of (a) the mean stress-intensity factor, $K_{I,m}$ and (b) the maximum dendrite length L_{max} with the surface energy density γ (3 – 4 $J\ m^{-2}$), and variations of (c) $K_{I,m}$ and (d) K_{IC} with E_{SE} (50 – 175 GPa) for different magnitudes of γ. The insets in (d) are the variations of L_{max} with E_{SE} in the stable and unstable regimes.

Fig. 9. Effect of SE surface compression, F_a (0 – 100 MPa): (a, b, and c) variations of $tr(\boldsymbol{\sigma})$, K_I and $\Delta\varphi$ with the dendrite length, L, respectively, (d) variations of $\Delta\varphi_m$ and $K_{I,m}$ with F_a, and (e) the variation of L_{max} with F_a and E_{SE}.

Table

Table 1 Governing equations of the PF model

Governing equation of SE fracture and lithium deposition	$\frac{\partial \phi}{\partial t} = -L_{\text{int}}\left(W\frac{\partial g(\phi)}{\partial \phi} - \gamma_0\delta_0\left(\begin{array}{l} \eta^2\nabla^2\phi - \\ \frac{\partial}{\partial x}\left(\eta\frac{\partial \eta}{d\theta}\frac{\partial \phi}{\partial y}\right) + \frac{\partial}{\partial y}\left(\eta\frac{\partial \eta}{d\theta}\frac{\partial \phi}{\partial x}\right) \end{array} \right) - \frac{\partial h(\phi)}{\partial \phi}\left(-\frac{\partial \psi^{\text{mech}}}{\partial \phi}\right) \right)$ $+\frac{\partial h(\phi)}{\partial \phi}L_{\text{bulk}}\left(a_{\text{R}}\exp\left(\frac{(1-\alpha)\left(\mu_{\text{R}}^{\text{ex}} - \mu_{\text{P}}^{\text{ex}}\right)}{RT}\right) - a_{\text{P}}\exp\left(-\frac{\alpha\left(\mu_{\text{R}}^{\text{ex}} - \mu_{\text{P}}^{\text{ex}}\right)}{RT}\right)\right)$
Governing equation of lithium diffusion	$\tau\frac{\partial \mu_{\text{Li}}}{\partial t} = \nabla\left(\frac{D_{\text{Li}}}{RT}\left(\begin{array}{l} h(\phi)c_{\text{Li,S}}^{\text{ref}}\exp\left(\frac{\mu_{\text{Li}} - \mu_{\text{Li,S}}^{0}}{RT}\right) + \\ (1-h(\phi))c_{\text{Li}^+,\text{SE}}^{\text{ref}}\exp\left(\frac{\mu_{\text{Li}} - \mu_{\text{Li}^+,\text{SE}}^{0}}{RT}\right) \end{array} \right)\left(\nabla\mu_{\text{Li}} + F\nabla\varphi_{\text{SE}}\right) \right)$ $-\frac{\partial h(\phi)}{\partial \phi}\left(c_{\text{Li,S}}^{\text{ref}} - c_{\text{Li}^+,\text{SE}}^{\text{ref}}\right)\exp\left(\frac{\mu_{\text{Li}}}{RT}\right)\frac{\partial \phi}{\partial t}$
Governing equation of electropotential field	$\nabla(\varepsilon\nabla\varphi) = Fc_{\text{Li,S}}^{\text{ref}}\frac{\partial \phi}{\partial t}$

Supplementary information:

Mechano-electrochemical modeling of lithium dendrite penetration in a solid-state electrolyte: mechanism and suppression

Chen Lin[a, *], Ling Xiong[a], Haihui Ruan[b, *]

a. Sino-French Institute of Nuclear Engineering and Technology, Sun Yat-Sen University, Zhuhai, China

b. Department of Mechanical Engineering, The Hong Kong Polytechnic University, Hong Kong, China

[*]Corresponding author Email: linch67@mail.sysu.edu.cn

[*]Corresponding author Email: haihui.ruan@polyu.edu.hk

[*] Corresponding author Tel.: + 86 15319738241, E-mail address: linch67@mail.sysu.edu.cn

[*] Corresponding author Tel.: + 852 2766 6648, Fax: +852 2365 4703, E-mail address: haihui.ruan@polyu.edu.hk

1. Note 1: Methodology in details

A sketch of lithium dendrite penetration in a solid-state electrolyte (SE) is shown in Fig. S1. The simplified electrochemical reaction for lithium deposition is expressed as: $Li^+ + e^- \rightarrow$ Li.

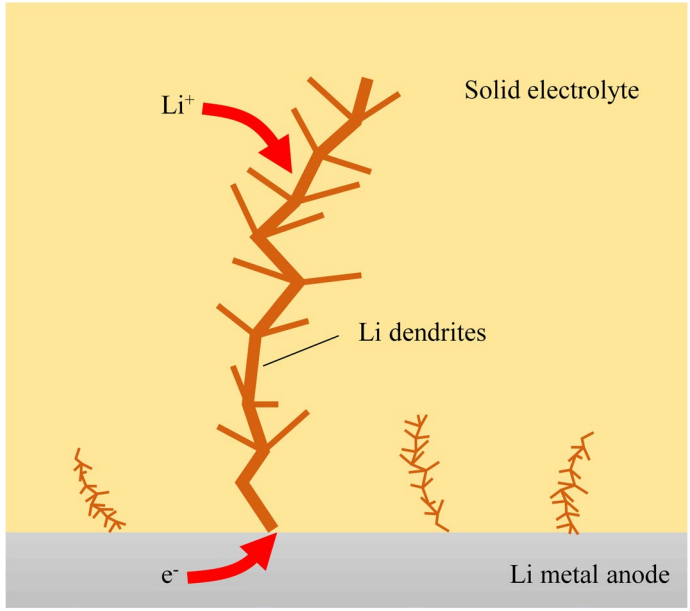

Fig. S1 Sketch of lithium dendrite penetration in ASSB

1.1. Helmholtz free energy for the lithium-SE system

The Helmholtz free energy of the system, Ψ, can be expressed as an integral of the density functional, ψ, over the domain, Ω, that is:

$$\Psi = \int_\Omega \psi dv = \int_\Omega \left(\psi^{\text{chem}} + \psi^{\text{elec}} + \psi^{\text{int}} + \psi^{\text{mech}} \right) dv \tag{S1}$$

where ψ is further split into chemical, electric, interfacial and mechanical potential densities, denoted by ψ^{chem}, ψ^{elec}, ψ^{int}, and ψ^{mech}, respectively. ψ^{chem} is expressed as a sum of the atomic lithium in deposit (S) and the ionic lithium in SE:

$$\psi^{\text{chem}} = \left(c_{\text{Li,S}} RT \left(\ln \frac{c_{\text{Li,S}}}{c_{\text{Li,S}}^{\text{ref}}} - 1 \right) + c_{\text{Li,S}} \mu_{\text{Li,S}}^0 \right) + \left(c_{\text{Li}^+,\text{SE}} RT \left(\ln \frac{c_{\text{Li}^+,\text{SE}}}{c_{\text{Li}^+,\text{SE}}^{\text{ref}}} - 1 \right) + c_{\text{Li}^+,\text{SE}} \mu_{\text{Li}^+,\text{SE}}^0 \right), \tag{S2}$$

The electric potential density, ψ^{elec}, resulting from the contribution of charged ions (Li^+) and electrons (e^-) in the system, is expressed as:

$$\psi^{elec} = F\varphi_{SE}c_{Li^+,SE} - F\varphi_S c_{e^-}. \tag{S3}$$

The interfacial energy density, ψ^{int}, corresponding to the energy consumed in the creation of a unit surface of the deposition, is expressed as:

$$\psi^{int} = \frac{\lambda}{2}|\nabla\phi|^2 + Wg(\phi), \tag{S4}$$

where the first term on the right-hand side is associated with the gradient of the order parameter (or phase identification), ϕ, in a diffusive interface with a finite width, and the second term is the double well function of $Wg(\phi) = W\phi^2(1-\phi)^2$ giving an energy barrier to ensure that the phases on both sides of an interface are stable. The coefficients W and λ can be related as $W = \gamma/(2\delta)$ and $\lambda = \gamma\delta$ based on the Griffith criterion [1], where γ is the Griffith energy density, i.e., the energy consumed in the creation of a unit area of fracture surface; δ denotes the thickness of a diffusive interface, which can be regarded as a pure numerical parameter or an actual material parameter determined from experiments [1]. Considering the orientation of lithium lattice, the interface must be anisotropic, which leads to $\gamma = \gamma_0\eta(\theta)$ and $\delta = \delta_0\eta(\theta)$. The orientation-dependent parameter, η, can be expressed as $\eta = 1 + \zeta\cos(k(\theta - \theta_0))$ [2], where ζ is the strength of interfacial anisotropy, θ is the angle between normal direction of interface and the nominal axis of system, θ_0 represent the fastest fracture direction that is consistent with the growth direction of lithium dendrite and k specifies the mode number that would be set as $k = 4$, because the lithium lattice has a cubic structure.

According to the first principles calculations by Fu *et al*. [3], the lithium ions dissolved interstitially in SE leads to a stoichiometric expansion in lattice of SE. In analogy to the thermal expansion coefficient, in numerical studies, the stoichiometric expansion, $\boldsymbol{\varepsilon}^{\mathrm{st}}$, can be expressed as:

$$\boldsymbol{\varepsilon}^{\mathrm{st}} = V_a c_{\mathrm{Li}^+,\mathrm{SE}} \mathbf{I}, \tag{S5}$$

where V_a is the partial molar volume change resulting from the expansion in lattice of SE by the dissolved lithium ions, which has been calculated based on first-principles simulations [3]. For the initial state that ASSBs without any deposited lithium and the distribution of lithium ions is uniform in SE, such a stoichiometric expansion, in analogy to the unconstrained isotropic thermal expansion, results in an initial stress-free state.

According to Barai *et al*. [4], once the lithium electrodeposition, the excess electrons can be trapped around the lanthanum (La) atoms located near the surface of the cubic LLZO, having the capability to reduce lithium ions and form lithium precipitates inside SE, which leads to a localized volumetric change in SE by the deposited lithium atoms than that by dissolved lithium ions. Such a localized volumetric change is constrained by surrounding SEs resulting in the stress building-up. In addition, the creep behavior of lithium has been experimentally studied in Ref. [5], which is believed to be important to the stress evolution. Thus, the mechanical energy density under the assumptions of isotropy and small deformation is expressed as:

$$\psi^{\mathrm{mech}} = \frac{1}{2}\left(\left(\boldsymbol{\varepsilon}^{\mathrm{e}}\right)^T \cdot \boldsymbol{\sigma}\right), \tag{S6}$$

where $\boldsymbol{\varepsilon}^{\mathrm{e}}$ and $\boldsymbol{\sigma}$ are, respectively, elastic strain and stress tensors. By considering the localized volumetric change in SE by the deposited lithium atoms than that by dissolved lithium ions and the creep behavior of lithium, elastic strain $\boldsymbol{\varepsilon}^{\mathrm{e}}$ can be further expressed as:

$$\boldsymbol{\varepsilon}^{\mathrm{e}} = \boldsymbol{\varepsilon} - \boldsymbol{\varepsilon}^{\mathrm{eg}} - \boldsymbol{\varepsilon}^{\mathrm{c}} \tag{S7}$$

where $\boldsymbol{\varepsilon}$, $\boldsymbol{\varepsilon}^{\mathrm{eg}}$, $\boldsymbol{\varepsilon}^{\mathrm{c}}$ are, respectively, the total strain, the volumetric eigenstrain and the creep strain. And the the constitutive relationship between stress and strain leads to the stress tensor is expressed as:

$$\boldsymbol{\sigma} = \mathbf{D}^{\mathrm{e}}\boldsymbol{\varepsilon}^{\mathrm{e}} = \mathbf{D}^{\mathrm{e}}\left(\boldsymbol{\varepsilon} - \boldsymbol{\varepsilon}^{\mathrm{eg}} - \boldsymbol{\varepsilon}^{\mathrm{c}}\right) \tag{S8}$$

where $\mathbf{D}^{\mathrm{e}}$ is the stiffness matrix expressed as $\mathbf{D}^{\mathrm{e}} = h(\phi)\mathbf{D}_{\mathrm{S}}^{\mathrm{e}} + \left(1 - h(\phi)\right)\mathbf{D}_{\mathrm{SE}}^{\mathrm{e}}$ to mollify the material discontinuity across the interface. It is note that since the stoichiometric expansion leads to an initial stress-free state for the initial uniform distribution of lithium ions and the deposited-lithium-free state in SEs, the stoichiometric expansion, $\boldsymbol{\varepsilon}^{\mathrm{st}}$, do not have the impact on stress evolution, which is not involved in the constitutive relationship.

Following geometric relation, the total strain, $\boldsymbol{\varepsilon}$, can be expressed as:

$$\boldsymbol{\varepsilon} = \left\{\varepsilon_{ij}\right\} = \left\{\frac{1}{2}\left(\frac{\partial d_i}{\partial x_j} + \frac{\partial d_j}{\partial x_i}\right)\right\} \ \left(i = 1,2,3;\ j{=}1,2,3\right). \tag{S9}$$

where d_i is the ith component of displacement field. The volumetric eigenstrain tensor, $\boldsymbol{\varepsilon}^{\mathrm{eg}}$, is expressed as:

$$\boldsymbol{\varepsilon}^{\mathrm{eg}} = p(\phi)\begin{bmatrix} \varepsilon_{11}^{\mathrm{eg}} & & \\ & \varepsilon_{22}^{\mathrm{eg}} & \\ & & \varepsilon_{33}^{\mathrm{eg}} \end{bmatrix}, \tag{S10}$$

where $\varepsilon_{11}^{\mathrm{eg}}$, $\varepsilon_{22}^{\mathrm{eg}}$, $\varepsilon_{33}^{\mathrm{eg}}$ are the components of the tensor. If the volumetric change is isotropic,

the components of the eigenstrain tensor can be expressed as $\varepsilon_{11}^{\mathrm{eg}} = \varepsilon_{22}^{\mathrm{eg}} = \varepsilon_{33}^{\mathrm{eg}} = \varepsilon_{\mathrm{m}}^{\mathrm{eg}}$.

Creep is described by the Norton power law:

$$\frac{d\varepsilon_{\mathrm{eq}}^{\mathrm{cr}}}{dt} = A\exp\left(-\frac{Q}{RT}\right)\left(\frac{\sigma^{\mathrm{eq}}}{\sigma_{\mathrm{ref}}}\right)^{m}, \tag{S11}$$

where $\varepsilon_{\mathrm{eq}}^{\mathrm{cr}}$ and σ^{eq} denote equivalent strain and equivalent stress, respectively; σ_{ref}, A and Q, m are parameters, denoting the reference stress, creep rate coefficient, activity energy of creep, and stress exponent of lithium, respectively.

By considering the static equilibrium condition, the stress tensor satisfies the equilibrium equation:

$$\mathrm{div}\left(\boldsymbol{\sigma}\right) = 0, \tag{S12}$$

where div is the divergence operator. Substituting Eqs. (S8), (S9) into Eq. (S12) leads to the governing equation of the mechanical deformation:

$$\mathrm{div}\left[\mathbf{D}^{\mathrm{e}}\left(\left\{\frac{1}{2}\left(\frac{\partial d_i}{\partial x_j} + \frac{\partial d_j}{\partial x_i}\right)\right\} - \boldsymbol{\varepsilon}^{\mathrm{eg}} - \boldsymbol{\varepsilon}^{\mathrm{c}}\right)\right] = 0. \tag{S13}$$

1.2 Electrochemical reaction kinetics for the lithium deposition

For a generalized reaction, the reaction rate, r, can be defined as:

$$r = k^{0}\left(\exp\left(-\frac{\mu_{\mathrm{TS}} - \mu_{\mathrm{R}}}{RT}\right) - \exp\left(-\frac{\mu_{\mathrm{TS}} - \mu_{\mathrm{P}}}{RT}\right)\right), \tag{S14}$$

where μ_{R}, μ_{P} and μ_{TS} are the chemical potentials of reactants and products and the chemical potential at the transition state, respectively. For a reaction involving multiple reactants and products, μ_{R} and μ_{P} can be expressed as:

$$\mu_{\mathrm{R}} = RT\ln\left(\prod_{\mathrm{i}}\left(a_{\mathrm{R_i^{X_i}}}\right)^{n_{\mathrm{i}}}\right)+\sum_{\mathrm{i}} n_{\mathrm{i}}\mu_{\mathrm{R_i^{X_i}}}^{\mathrm{ex}}\ , \tag{S15a}$$

$$\text{and}\ \ \mu_{\mathrm{P}} = RT\ln\left(\prod_{\mathrm{j}}\left(a_{\mathrm{P_j^{Z_j}}}\right)^{m_{\mathrm{j}}}\right)+\sum_{\mathrm{j}} m_{\mathrm{j}}\mu_{\mathrm{P_j^{Z_j}}}^{\mathrm{ex}}\ . \tag{S15b}$$

where denoted by $\mathrm{R_i}$ and $\mathrm{P_j}$ are reactants and products, respectively, n_{i} (or m_{j}) and $\mathrm{X_i}$ (or $\mathrm{Z_j}$) the stoichiometric number and charge number, respectively, and a_* and μ_*^{ex} the activity and the excess chemical potential of $*$, respectively. According to Bazant [6], the activity is only concentration dependent, defined as:

$$a_* = \exp\left(\frac{1}{RT}\left(\frac{\delta\left(\int_\Omega\left(\psi^{\mathrm{chem}}+\psi^{\mathrm{int}}\right)d\omega\right)}{\delta c_*}-\mu_*^0\right)\right). \tag{S16}$$

Correspondingly, the excess chemical potential, μ_*^{ex}, is:

$$\mu_*^{\mathrm{ex}} = \frac{\delta\left(\int_\Omega\left(\psi-\psi^{\mathrm{chem}}-\psi^{\mathrm{int}}\right)d\omega\right)}{\delta c_*}+\mu_*^0, \tag{S17}$$

which involves the contributions of mechanical energy, electric potential, and standard chemical potential. The chemical potential at the transition state, μ_{TS}, is defined as:

$$\mu_{\mathrm{TS}} = RT\ln a^{\mathrm{TS}} + \alpha\sum_{\mathrm{i}} n_{\mathrm{i}}\mu_{\mathrm{R_i^{X_i}}}^{\mathrm{ex}} + (1-\alpha)\sum_{\mathrm{j}} n_{\mathrm{j}}\mu_{\mathrm{P_j^{Z_j}}}^{\mathrm{ex}}\ , \tag{S18}$$

Substituting Eqs. (S15 – S18) into Eq. (S14) and involving the detailed expressions of energy densities (Eqs. (S2–S5)), the reaction rate, r, can be finally derived as:

$$r = \frac{k^0}{a^{\mathrm{TS}}}\left(a_{\mathrm{R}}\exp\left(\frac{(1-\alpha)\left(\mu_{\mathrm{R}}^{\mathrm{ex}}-\mu_{\mathrm{P}}^{\mathrm{ex}}\right)}{RT}\right)-a_{\mathrm{P}}\exp\left(-\frac{\alpha\left(\mu_{\mathrm{R}}^{\mathrm{ex}}-\mu_{\mathrm{P}}^{\mathrm{ex}}\right)}{RT}\right)\right), \tag{S19}$$

where the activity of reactants and products, a_{R} and a_{P}, are, respectively, expressed as:

$$a_{\mathrm{R}} = \prod_{\mathrm{i}}\left(a_{\mathrm{R_i^{X_i}}}\right)^{n_{\mathrm{i}}} = \frac{c_{\mathrm{Li^+,SE}}}{c_{\mathrm{Li^+,SE}}^{\mathrm{ref}}}\ \ \text{and} \tag{S20a}$$

$$a_{\mathrm{P}} = \prod_{\mathrm{j}} \left(a_{\mathrm{P_j^{Z_j}}} \right)^{m_{\mathrm{j}}}$$
$$= \exp\left[\frac{1}{RTc_{\mathrm{Li,S}}^{\mathrm{ref}}} \left(W \frac{\partial g(\phi)}{\partial \phi} - s_0 \delta_0 \left(\begin{array}{l} \eta(\theta)^2 \nabla^2 \phi - \\ \frac{\partial}{\partial x}\left(\eta(\theta) \frac{\partial \eta(\theta)}{d\theta} \frac{\partial \phi}{\partial y} \right) + \frac{\partial}{\partial y}\left(\eta(\theta) \frac{\partial \eta(\theta)}{d\theta} \frac{\partial \phi}{\partial x} \right) \end{array} \right) \right) \right] + \frac{c_{\mathrm{Li,S}}}{c_{\mathrm{Li,S}}^{\mathrm{ref}}},$$

(S20b)

and the excess chemical potential of reactants and products, $\mu_{\mathrm{R}}^{\mathrm{ex}}$ and $\mu_{\mathrm{P}}^{\mathrm{ex}}$ are, respectively, expressed as:

$$\mu_{\mathrm{R}}^{\mathrm{ex}} = \mu_{\mathrm{Li^+,SE}}^{0} + F\left(\varphi_{\mathrm{SE}} - \varphi_{\mathrm{S}}\right) \text{ and} \tag{S21a}$$

$$\mu_{\mathrm{P}}^{\mathrm{ex}} = \mu_{\mathrm{Li,S}}^{0} - \frac{1}{c_{\mathrm{Li,S}}^{\mathrm{ref}}} h(\phi) \varepsilon^{\mathrm{eg}} \mathrm{tr}(\boldsymbol{\sigma}) - \frac{\partial h(\phi)}{2c_{\mathrm{Li,S}}^{\mathrm{ref}} \partial \phi} \left(\boldsymbol{\varepsilon}^{\mathrm{e}}\right)^{T} \left(\left(\mathbf{D}_{\mathrm{SE}}^{\mathrm{e}} - \mathbf{D}_{\mathrm{S}}^{\mathrm{e}} \right) \boldsymbol{\varepsilon}^{\mathrm{e}} \right). \tag{S21b}$$

Considering the hydrostatic-stress-dependence on the chemical potential for the species diffusion proposed by Larché and Cahn [7], the excess chemical potential of reactants (Eq. (S21a)) can be recast as:

$$\mu_{\mathrm{R}}^{\mathrm{ex}} = \mu_{\mathrm{Li^+,SE}}^{0} + F\left(\varphi_{\mathrm{SE}} - \varphi_{\mathrm{S}}\right) - \left(1 - h(\phi)\right) V_a \mathrm{tr}(\boldsymbol{\sigma}). \tag{S22}$$

Thus, the difference of excess chemical potential, $\mu_{\mathrm{R}}^{\mathrm{ex}} - \mu_{\mathrm{P}}^{\mathrm{ex}}$, can be expressed as Eq. (2). The Since the cracked region is assumed to be filled with lithium, the dimensionless concentration of atomic lithium in deposit, $c_{\mathrm{Li,S}} / c_{\mathrm{Li,S}}^{\mathrm{ref}}$, can be associated with the order parameter, ϕ, i.e., $c_{\mathrm{Li,S}} / c_{\mathrm{Li,S}}^{\mathrm{ref}} = \phi$.

1.3 Governing equation of dendrite penetration in ASSB

In present work, the interfacial migration in SE is attributed to the mechanical cracking

and lithium electrodeposition, thus its migration rate, $\partial\phi/\partial t$, is divided into two terms:

$$\frac{\partial\phi}{\partial t} = -L_{\text{int}}\frac{\delta\Psi}{\delta\phi} - \frac{\partial h(\phi)}{\partial\phi}\frac{r}{c_{\text{Li,S}}^{\text{ref}}}. \tag{S23}$$

The first term on the right-hand side of Eq. (S23) describes mechanical cracking induced by stress, which is in the form of the Allen–Cahn equation to minimize the free energy of the system. More specifically, it is expressed as,

$$-L_{\text{int}}\frac{\delta\Psi}{\delta\phi} = -L_{\text{int}}\left(W\frac{\partial g(\phi)}{\partial\phi} - s_0\delta_0\left(\eta^2\nabla^2\phi - \frac{\partial}{\partial x}\left(\eta\frac{\partial\eta}{d\theta}\frac{\partial\phi}{\partial y}\right) + \frac{\partial}{\partial y}\left(\eta\frac{\partial\eta}{d\theta}\frac{\partial\phi}{\partial x}\right)\right) - \frac{\partial h(\phi)}{\partial\phi}\left(-\frac{\partial\psi^{\text{mech}}}{\partial\phi}\right)\right). \tag{S24}$$

The second term on the right-hand side of Eq. (S23) represents the interfacial evolution resulting from the lithium electrodeposition. Note that the interface can be regarded as an area with Li atoms, cations, and damaged SE, that is we assumed a finite width of overlapping between lithium and SE in order to deal with contact problem between the two solid-state phases. The electrodeposition can drive this interface to migrate of a certain level, i.e., lithium deposit should push away SE. Such an interface evolution is associated with the electrodeposition reaction rate; therefore, it is expressed as follows:

$$-\frac{\partial h(\phi)}{\partial\phi}\frac{r}{c_{\text{Li,S}}^{\text{ref}}} = \frac{\partial h(\phi)}{\partial\phi}L_{\text{bulk}}\left(a_{\text{R}}\exp\left(\frac{(1-\alpha)\left(\mu_{\text{R}}^{\text{ex}} - \mu_{\text{P}}^{\text{ex}}\right)}{RT}\right) - a_{\text{P}}\exp\left(-\frac{\alpha\left(\mu_{\text{R}}^{\text{ex}} - \mu_{\text{P}}^{\text{ex}}\right)}{RT}\right)\right), \tag{S25}$$

where the coefficient, $L_{\text{bluk}} = k_0/a_{\text{TS}}c_{\text{Li,S}}^{\text{ref}}$, is to scale the contribution of electrodeposition

kinetics to interface migration. Substituting Eqs. (S24) and (S25) into Eq. (S23) leads to Eq. (1) in the main text.

1.4 Governing equation of diffusion of lithium cations

With the concentration of lithium atoms, $c_{\mathrm{Li,S}}$, in the deposit and that of lithium cations, $c_{\mathrm{Li^+,SE}}$, in the electrolyte, the concentration of lithium species, c_{Li}, in the interface can be treated as an interpolation of $c_{\mathrm{Li,S}}$ and $c_{\mathrm{Li^+,SE}}$ [8], i.e.,

$$c_{\mathrm{Li}} = h(\phi)c_{\mathrm{Li,S}} + \left(1-h(\phi)\right)c_{\mathrm{Li^+,SE}}, \tag{S26}$$

where $c_{\mathrm{Li,S}}$ and $c_{\mathrm{Li^+,SE}}$ are related by the following equation based on the KKS model [8]:

$$\frac{\partial \psi^{\mathrm{chem}}}{\partial c_{\mathrm{Li,S}}} = \frac{\partial \psi^{\mathrm{chem}}}{\partial c_{\mathrm{Li^+,SE}}} = \mu_{\mathrm{Li}}, \tag{S27}$$

i.e., the chemical potentials of lithium atom and cation are equal in the diffusive interface as they coexist. This is the so-called quasi-equilibrium condition, which leads to the following expressions of $c_{\mathrm{Li,S}}$ and $c_{\mathrm{Li^+,SE}}$:

$$c_{\mathrm{Li,S}} = c_{\mathrm{Li,S}}^{\mathrm{ref}} \exp\left(\frac{\mu_{\mathrm{Li}} - \mu_{\mathrm{Li,S}}^{0}}{RT}\right) \tag{S28a}$$

$$\text{and } c_{\mathrm{Li^+,SE}} = c_{\mathrm{Li^+,SE}}^{\mathrm{ref}} \exp\left(\frac{\mu_{\mathrm{Li}} - \mu_{\mathrm{Li^+,SE}}^{0}}{RT}\right). \tag{S28b}$$

Because the electrochemical reaction in the interface consumes the lithium cations and simultaneously produces lithium atoms, lithium species (cations and atoms) must be conserved. Thus, the mass conservation law leads to the following diffusion equation of lithium species:

$$\frac{\partial c_{\mathrm{Li}}}{\partial t} = -\nabla \mathbf{j}. \tag{S29}$$

where $\mathbf{j}$ is the molar flux of lithium species per unit area regulated by the gradients of chemical

potential and electric fields, i.e., the Nernst-Planck equation:

$$\mathbf{j} = -\frac{D_{\mathrm{Li}} c_{\mathrm{Li}}}{RT}\left(\nabla \mu_{\mathrm{Li}} + F \nabla \phi\right). \tag{S30}$$

Substituting Eqs. (S26, S28, S30) into Eq. (S29) leads to the equation governing lithium diffusion in the system, i.e., Eq. (3a) in the main text.

2. Note 2: Boundary conditions and material parameters in simulation

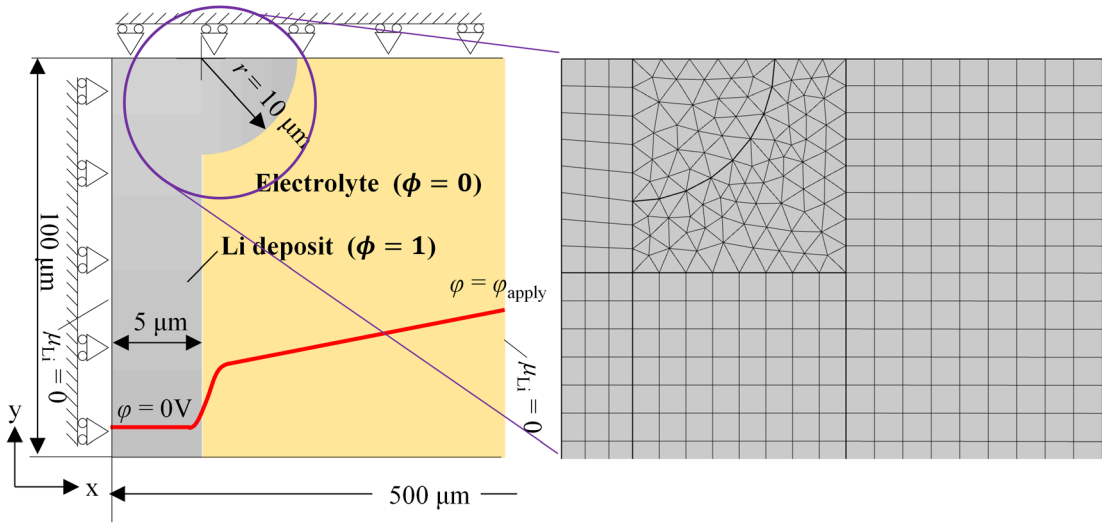

Fig. S2 Boundary conditions of the simulation domain with FE meshes

In the present work, a two-dimensional domain with the size of 100 μm × 500 μm is employed for the binary-phase system consisting of Li deposit ($\phi = 1$) and SE ($\phi = 0$). And the Li deposit-SE interface for this binary-phase system is assumed to be flat but with a semi-circle hump of the radius of 10 μm. Owing to symmetry, only half of the domain is simulated, as shown in Fig. S2.

Since the chemical potential field rather than the concentration field is solved based on Eq. (3a), the initial and boundary conditions should be given in the form of chemical potential.

We assume that the deposits and SE are initially at a state of chemical equilibrium, therefore $\mu_{\mathrm{Li}} = 0$ at $t = 0$. The corresponding equilibrium concentrations of lithium atoms in the deposit and cations in SE is determined to be 76.4 and 4.22 $\mathrm{mol \cdot L^{-1}}$, respectively. Also, chemical equilibrium, $\mu_{\mathrm{Li}} = 0$, is imposed as a Dirichlet boundary condition on the left and right sides of the simulation domain. For the other sides, the zero-flux boundary condition, $\nabla\mu_{\mathrm{Li}} = 0$, is applied. For the electrical potential, the fixed potential difference boundary condition is applied, i.e., the Dirichlet boundary conditions $\varphi = 0$ and $\varphi = \varphi_{\mathrm{apply}}$ are set at the left and right sides, respectively; the zero-flux condition, $\nabla\varphi = 0$, is applied to the other sides. It is note that the fixed current boundary condition is also widely used in the practical application. Due to limited space, we do not used this condition in present simulation, but the way to produce the resulting fixed current is provide here, i.e., the Dirichlet boundary condition of $\mu_{\mathrm{Li}} = 0$, on the right sides of the simulation domain is replaced by a fixed flux boundary condition, $Fc^{\mathrm{ref}}_{\mathrm{Li^+,SE}} \nabla\left(\exp\left(\mu_{\mathrm{Li}}\right)\right) = \boldsymbol{I}_0$, where $\boldsymbol{I}_0$ is the applied fixed current. For mechanical deformation, the top side represents the axisymmetric axis of binary-phase system; the left and right are constrained along their normal direction; and the bottom side is constrained to remain straight and vertical, but it is allowed to move in the normal direction. The reference temperature in simulation is set at 293K.

To guarantee the convergence of the solution and achieve a reasonable computational efficiency, the simulation domain is discretized by employing the square mesh with a uniform element size of 2 μm (i.e., five times smaller than the interface thickness) and the triangular

mesh with maximum size of 2 μm, as shown in Fig. S2. The Newton–Raphson method is employed to solve the nonlinear governing equations, in which the time-step is automatically refined to ensure the convergence of the solution step. In our simulations, the initial and maximum time steps are, respectively, 10^{-6} t_{ref} and 10^{-3} t_{ref} for temporal integration, where t_{ref} is the reference time. The parameters used in simulation are listed in Table S1.

Table S1

	Parameter	Value
Reference length	l_{ref}	100 μm
Reference time	t_{ref}	1000 s
Interface thickness	δ	10 μm
interfacial energy density	γ	3 – 4 J m^{-2}
Fracture toughness of SE	K_{IC}	1.07–1.24 MPa $m^{0.5}$ (See Eq. S26)
Strength of interfacial anisotropy	ζ	0.02
The fastest growth direction	θ_0	0
The mode number to represent the cubic structure of lithium lattice	k	4
Young's modulus of the lithium	E_S	4.9 GPa [9]
Young's modulus of the SE	E_{SE}	50 – 175 GPa [9]
Poisson's ratio of the lithium	ν_S	0.4 [10]

Poisson's ratio of the SE	ν_{SE}	0.257 [9]
Component of volumetric eigenstrain	ε_m^{eg}	0.008–0.012
Partial mole volume change resulting from the increasing fraction of diffusive lithium cation dissolved interstitially in the host lattice of SE	V_a	0.5–6 cm^3 mol^{-1}[3]
Activity energy of lithium for creep	Q	37 KJ mol^{-1}[5]
Stress exponent of lithium for creep	m	6.6[5]
Creep rate coefficient of lithium	$A^{-1/m}$	3×10^{-5} Pa s^{-1}[5]
Reference concentration of lithium	$c_{Li,S}^{ref}$	76.4 mol L^{-1} [11]
Reference concentration of lithium ion in SE	$c_{Li^+,SE}^{ref}$	4.22 mol L^{-1} [12]
Standard chemical potential of lithium	$\mu_{Li,S}^0$	0
Standard chemical potential of lithium ion in electrolyte	$\mu_{Li^+,SE}^0$	0
Coefficients to scale the contributions of interfacial energy to phase migration	L_{int}	1.2×10^{-7} m^3 J^{-1} s^{-1}
Coefficient to scale the contributions of the deposition kinetics to phase migration	L_{bluk}	0.6 s^{-1}

Asymmetry factor	α	0.5 [14]
Diffusion coefficient of atomic lithium in lithium	D_S	6×10^{-15} m^2 s^{-1} [13]
Diffusion coefficient of ionic lithium in SE	D_{SE}	6×10^{-12} m^2 s^{-1} [13]
Electric conductivity of SE	ε_{SE}	1 S m^{-1} [14]
Electric conductivity of lithium deposit	ε_S	10^7 S m^{-1} [14]
Ideal gas constant	R	8.314 J mol^{-1} K^{-1}
charge number of lithium ion	n	1
Faraday's constant	F	96485 C mol^{-1}

It is note that in table S1 value of eigenstrain is still not accurately determined by experimental or numerical studies. And it is different in different studies. For example, in Tantratian *et al*.'s model [13], the eigenstrain is regards to be anisotropic, which is expressed in form of a matrix as:

$$\mathbf{K_{ii}} = \begin{bmatrix} K_{11} & & \\ & K_{22} & \\ & & K_{33} \end{bmatrix}, \tag{S32}$$

where the components $K_{11} = K_{22} = 5 \times 10^{-5}$ and $K_{33} = 2 \times 10^{-4}$. In their model, the creep behavior of lithium is not considered. Thus, such a small value of eigenstrain is set to stratify the estimation of Von mises stress level falling within the order of a few MPa in lithium. Due to the nature of electrochemical reaction in a solid system, the mechanical stress should play a critical role in governing the Li deposition rate. However, such a small value of eigenstrain

have no material effect on the electrodeposition reaction. Thus, an extra coefficient, C, is introduced in their model to artificially amplify the effect of stress on reaction. In Monroe *et al*. [11], Ahmad *et al*. [12], Porz *et al*. [15] and Klinsmann *et al*. [16] models, a very large value of eigenstrain of 1 is set, which causes the stress in SEs reaching quickly to a few to more than ten GPa, which is too large for a brittle materials.

Thus, in present simulation, the median eigenstrain of 0.008 ~ 0.012 is set, which is larger than that in Tantratian *et al*.'s model [13] but smaller than that in Monroe *et al*. [11], Ahmad *et al*. [12], Porz *et al*. [15] and Klinsmann *et al*. [16] models. It causes the stress level fall within a reasonable range of a few MPa in lithium and the hundreds MPa to about 1 GPa in SEs. And it also has the material effect on the electrodeposition reaction without an extra coefficient to amplify its influence.

3. Note 3

The stress-intensity factor for mode-I crack, K_{I}, can be calculated based on the strain energy release rate as follows:

$$K_{\mathrm{I}} = \sqrt{-\frac{E}{t_{\mathrm{s}}}\partial\left(\int_{\Omega}\psi^{\mathrm{mech}}dv\right)\Big/\partial L}\,, \tag{S31}$$

where $t_{\mathrm{s}} = l_{\mathrm{ref}}$ is the thickness of the sample, and $-\partial\left(\int_{\Omega}\psi^{\mathrm{mech}}dv\right)\Big/\left(t_{\mathrm{s}}\partial d_{\mathrm{c}}\right)$ is the strain energy release rate with an increase in the crack length, L.

According the Yuan *et al*.[9], the fracture toughness, K_{IC}, can be expressed as:

$$K_{\mathrm{IC}} = \sqrt{\frac{E_{\mathrm{SE}}\gamma}{2\left(1-\nu_{\mathrm{SE}}{}^{2}\right)}}\,, \tag{S32}$$

where E_{SE} , ν_{SE} and γ are, respectively, the the Young's module, Poisson's ratio and the surface energy density of SE.

References

[1] T.-T. Nguyen, J. Yvonnet, M. Bornert, C. Chateau, K. Sab, R. Romani, R.L. Roy, On the choice of parameters in the phase field method for simulating crack initiation with experimental validation, Int. J. Fract. 197 (2016) 213–226.

[2] J.M. Debierre, A. Karma, F. Celestini, R. Guerin, Phase-field approach for faceted solidification, Phys. Rev. E, 68 (2003) 041604.

[3] Z.H. Fu, X. Chen, C.Z. Zhao, H. Yuan, R. Zhang, X. Shen, X.X. Ma, Y. Lu, Q.B. Liu, L.Z. Fan, and Q. Zhang, Stress Regulation on Atomic Bonding and Ionic Diffusivity: Mechanochemical Effects in Sulfide Solid Electrolytes, Energy Fuels 35 (2021) 10210–10218.

[4] P. Barai, A.T. Ngo, B. Narayanan, K. Higa, L.A. Curtiss, V. Srinivasan, The role of local inhomogeneities on dendrite growth in LLZO-based solid electrolytes. J. Electrochem. Soc. 167 (2020) 100537.

[5] W.S. LePage, Y.X. Chen, E. Kazyak, K.H. Chen, A.J. Sanchez, A. Poli, E.M. Arruda, M. D. Thouless, N.P. Dasgupta, Lithium Mechanics: Roles of Strain Rate and Temperature and Implications for Lithium Metal Batteries, J. Elec. Soc. 166 (2019) A89–A97.

[6] M.Z. Bazant, Theory of chemical kinetics and charge transfer based on nonequilibrium thermodynamics, Acc Chem. Res., 46 (2013) 1144–1160.

[7] F. C. Larche, J. L. Cahn, The effect of self-stress on diffusion in solids, Acta Metall., 30 (1982) 1835–1845.

[8] S. G. Kim, W. T. Kim, and T. Suzuki, Phase-field model for binary alloys, Phys. Rev. E, 60 (1999) 7186.

[9] C.H. Yuan, W.Q. Lu, J. Xu, Unlocking the Electrochemical–Mechanical Coupling Behaviors of Dendrite Growth and Crack Propagation in All-Solid-State Batteries, Adv Energy Mater (2021) 2101807

[10] G. V. Samsonov, Handbook of the Physicochemical Properties of the Elements, New York 1968.

[11] C. Monroe, J. Newman, The effect of interfacial deformation on electrodeposition kinetics, J. Electrochem. Soc. 151 (2004) A880–A886.

[12] Z. Ahmad, V. Viswanathan, Stability of Electrodeposition at Solid-Solid Interfaces and Implications for Metal Anodes, Phys. Rev. Lett. 119 (2017) 056003.

[13] K. Tantratian, H.H. Yan, K. Ellwood, E.T. Harrison, L. Chen, Unraveling the Li Penetration Mechanism in Polycrystalline Solid Electrolytes, Adv. Energy Mater. 11 (2021) 2003417.

[14] L. Chen, H.W. Zhang, L.Y. Liang, Z. Liu, Y. Qi, P. Lu, J. Chen, L. Chen, Modulation ofdendritic patterns during electrodeposition: a nonlinear phase-field model, J. Power Sources 300 (2015) 376–385.

[15] L. Porz, T. Swamy, B.W. Sheldon, D. Rettenwander, T. Frmling, H.L. Thaman, S. Berendts, R. Uecker, W.C. Carter, Y.M. Chiang, Mechanism of lithium metal penetration through inorganic solid electrolytes, Adv Energy Mater 7 (2017) 1701003.

[16] M. Klinsmann, F.E. Hildebrand, M. Ganser, R.M. McMeeking, Dendritic cracking in solid electrolytes driven by lithium insertion, J Power Sources 442 (2019) 227226.